Advances in Water Resources 107 (2017) 32–42

Contents lists available at ScienceDirect

Advances in Water Resources

journal homepage: www.elsevier.com/locate/advwatres

# Statistical representative elementary volumes of porous media determined using greyscale analysis of 3D tomograms

S. Bruns*, S.L.S. Stipp, H.O. Sørensen

*Nano-Science Center, Department of Chemistry, University of Copenhagen, Universitetsparken 5, 2100 Copenhagen Ø, Denmark*

ARTICLE INFO

*Article history:*
Received 28 October 2016
Revised 18 May 2017
Accepted 8 June 2017
Available online 13 June 2017

*Keywords:*
Greyscale image analysis
Porous media properties
X-ray nanotomography
Representative elementary volume
Petrophysical parameters
Aquifer material

ABSTRACT

Digital rock physics carries the dogmatic concept of having to segment volume images for quantitative analysis but segmentation rejects huge amounts of signal information. Information that is essential for the analysis of difficult and marginally resolved samples, such as materials with very small features, is lost during segmentation. In X-ray nanotomography reconstructions of Hod chalk we observed partial volume voxels with an abundance that limits segmentation based analysis. Therefore, we investigated the suitability of greyscale analysis for establishing statistical representative elementary volumes (sREV) for the important petrophysical parameters of this type of chalk, namely porosity, specific surface area and diffusive tortuosity, by using volume images without segmenting the datasets. Instead, grey level intensities were transformed to a voxel level porosity estimate using a Gaussian mixture model. A simple model assumption was made that allowed formulating a two point correlation function for surface area estimates using Bayes' theory. The same assumption enables random walk simulations in the presence of severe partial volume effects. The established sREVs illustrate that in compacted chalk, these simulations cannot be performed in binary representations without increasing the resolution of the imaging system to a point where the spatial restrictions of the represented sample volume render the precision of the measurement unacceptable. We illustrate this by analyzing the origins of variance in the quantitative analysis of volume images, i.e. resolution dependence and intersample and intrasample variance. Although we cannot make any claims on the accuracy of the approach, eliminating the segmentation step from the analysis enables comparative studies with higher precision and repeatability.



## 1. Introduction

Digital rock physics makes it possible to estimate macroscopic petrophysical parameters and to explore fluid transport or dynamic deformation processes from volume images of a milli- or micrometer sized sample of a porous medium, such as reservoir rock (Arns et al., 2001; Bijeljic et al., 2013; Fredrich et al., 2006; Fusseis et al., 2014; Golab et al., 2013; Jouini et al., 2014; Knackstedt et al., 2009; Kynde et al., 2016; Mostaghimi et al., 2013; Raeini et al., 2015; Siddiqui and Sarker, 2010; Zhu et al., 2007; Bultreys et al., 2015; Lin et al., 2016; Mostaghimi et al., 2016; Shah et al., 2016; Smith et al., 2017). Such samples can be produced from the cuttings of rotary drilling. If information for characterizing reservoirs could be gained from drill cuttings, it would be 10 to 20 times less costly than drilling a dedicated exploration well for acquiring core plugs, such as are used in traditional evaluation. This makes digital rock physics attractive for evaluating the economic and technical feasibility of marginal oil reservoirs and for other applications where information about the internal structure of materials is essential.

Chalk is a frequent reservoir rock in the North Sea Basin. It is a very challenging material for digital rock physics because of its very fine grain size. Chalk is formed of the calcified shields of coccolithophorids, one celled, free floating algae. The individual elements of the coccoliths are submicrometer dimension and irregular in size, shape and orientation (Balogh et al., 2009). 3D imaging with resolution high enough to resolve the pores of chalk is required to provide reliable data for digital analysis and X-ray based nanotomography is certainly among the most feasible methods for accomplishing this. Yet, even nanotomography resolution is often not enough to clearly resolve all the features in fine grained material, such as the fractures and fine pore throats in a compacted chalk sample (Dalby et al., 2014). A comprehensive reservoir analysis cannot focus on chalk with oil production grade porosity alone (Hu et al., 2012). Recently, Dalby et al. (2014) advanced to imaging compacted chalk using ptychographic X-ray tomography (PXCT), with voxel dimension of 21.5 nm, but it is questionable whether such high resolution imaging is able to provide a statistical rep-

* Corresponding author.
*E-mail address:* bruns@nano.ku.dk (S. Bruns).

http://dx.doi.org/10.1016/j.advwatres.2017.06.002
0309-1708/

resentative elementary volume (sREV) for a compacted sample on the pore scale (Zhang et al., 2000).

The suitability of 3D imaging for evaluating the hydrodynamic and petrophysical parameters for chalk and other carbonate rocks has been addressed in recent publications (Andrä et al., 2013; Keller et al., 2013; Liu et al., 2014; Müter et al., 2014; Yoon and Dewers, 2013; Saraji and Piri, 2015; Kelly et al., 2016). In search of a statistically representative elementary volume, Yoon and Dewers (2013) evaluated the nanopore structure and transport properties of a Cretaceous Selma chalk where porosity ($\Phi$) was ~16%, using a FIB-SEM 3D image of a sample that was 15 µm × 15 µm × 8 µm. From downscaling, they concluded that a minimum of 80 nm voxel resolution would be required to avoid resolution dependence and that their sample was well represented with a volume of 10 µm × 10 µm × 10 µm. Unfortunately, their results cannot be extrapolated directly to all chalk types because tight chalks are far more heterogeneous and rely on fluid transport through microfractures (Zhu et al., 2007; Warren, 2000). Müter et al. (2014) specifically addressed resolution dependence in a tomography study of two highly compacted chalk samples ($\Phi = 0.04–0.07$) and a more porous sample ($\Phi \approx 0.28$). They reported that a voxel resolution of 25 nm, corresponding to an optical resolution of 150 nm, served well as an upper boundary for the tomographic characterization of chalk data. In 2015 *Saraji and Piri* published a high resolution FIB-SEM based study where they were concerned with finding a representative sample size for low porosity, carbonate containing, shale oil rocks from the Bakken formation (Saraji and Piri, 2015). While they succeeded in establishing a sREV for porosity the field of view was too small to identify a sREV for permeability. They questioned whether the limited field of view in FIB-SEM studies is sufficient for such an analysis and compared their result for porosity with representative elementary areas calculated from larger two dimensional SEM maps of their samples, which revealed porosity values quite different from their 3D analysis. *Kelly* et al. came to the same conclusion when assessing the permeability of shale via FIB-SEM. For volumes of 5000 µm$^3$ they found suitable values for porosity but the results of their permeability simulations varied by as much as three orders of magnitude (Kelly et al., 2016). They attributed this to the often unconnected pore morphology in the limited available field of view and advised caution in studying low porosity samples via a single FIB-SEM stack.

There are also studies that approach the sREV in carbonates from segmented tomography reconstructions with micrometer resolution thereby easily covering the millimeter scale (Mostaghimi et al., 2013; Zakirov et al., 2016). *Mostaghimi* et al. emphasized that the sREV for parameters that need to account for tortuosity and connectedness of the flow paths (permeability) are larger than for the static properties (porosity and specific surface area) (Mostaghimi et al., 2013). They considered a coarse grained carbonate sample with 14% porosity at 5.3 µm voxel resolution and a 23% porous sample at 2.85 µm resolution, concluding that the sREV is potentially larger than the 300 × 300 × 300 voxel image considered. The difference for the conclusions made in the above FIB-SEM studies is quite obvious. Low resolution imaging ignores matrix porosity and is prone to severe segmentation errors, i.e. only fracture heterogeneity can be captured in the analysis (laboratory scale) whereas high resolution imaging will focus on heterogeneities in the bulk matrix material which is much smaller (pore scale).

In a recent review article, Wildenschild and Sheppard (2013) described greyscale analysis as ideal in principle but too limited in available measurable parameters and in reproducibility, for practical purposes in quantitative image analysis. Therefore, a central processing step in the studies described above, and almost any quantitative study on microstructural characterization of porous systems, remains image segmentation (Iassonov et al., 2009; Müter et al., 2012). It is seen as a requirement for quantitative physical analysis and is usually performed as hard segmentation, using a thresholding criterion, such as the Otsu threshold. Implementation is fast and simple, but it is well known that problems are associated with using thresholded images for quantitative analysis. For example, even for an image with a homogeneous point spread function and uniform illumination, an object that is smaller than ten times the image resolution is only delineated correctly with a single threshold value if it is spherical (Lee, 2010). Obviously, this requirement is not fulfilled in samples with complex microstructures. The situation worsens when compacted samples are analyzed because in these materials, microfractures contribute considerably to the transport properties of the pore system (Zhu et al., 2007; Warren, 2000). With marginally insufficient resolution, fractures only appear as partial volume voxels and therefore, they are incorrectly assigned to the materials phase so segmentation errors cannot be expected to even out statistically but result in a loss of pore connectivity. The signal information for the fractures that was originally contained in the greyscale is lost.

Given the pronounced disparity between the proportions of the material and the void phases in compacted chalk, it is not surprising that such samples are far more heterogeneous than chalk samples with a more open pore network. Heterogeneity has to be countered by increasing the amount or the volume of the measurements, leaving us with a sample that requires both a large sampled volume and a high signal resolution. In most applications, with the possible exception of serial block-face scanning electron microscopy (Denk and Horstmann, 2004; Müllner et al., 2014), which is most suited for softer materials, these requirements are mutually exclusive and a compromise has to be made. Available detectors cap the size of imaged features in synchrotron imaging at roughly 500 times the signal resolution and an extensive number of repetitions in a nanotomography experiment is out of the range of possibility for any funding or beamtime proposal. Consequently, it is of elevated interest to establish sREVs such that imaging experiments can be designed in a way that minimizes the combined uncertainty resulting from spatial resolution and limited field of view.

In chalk or any very fine grained material, the number of partial volume voxels is significant and a tomographic reconstruction with a bimodal, well segmentable intensity distribution is rather the exception than the rule. Consequently, it is desirable, if not mandatory, to incorporate signal information from partial volume voxels in the analysis of petrophysical parameters (i) to arrive at a comprehensive reservoir characterization and (ii) to avoid unpredictable reservoir behavior.

In this study, we investigated the suitability of greyscale analysis for chalk tomography reconstructions, imaged at varying spatial resolution, for establishing sREVs that bridge the gap between high and low resolution imaging experiments. We illustrate how greyscale intensities in computed tomography (CT) reconstructions of chalk can be transferred to a material density representation that is comparable between samples and we calculate porosity, specific surface area and diffusive tortuosity, without image segmentation. A workaround was required to approximate the unresolved subvoxel pore structure and to enable quantitative evaluation of parameters that relate to the pore surface and available flow paths. Without claiming accuracy for this approximation, precision and repeatability are maintained, which is essential for a comparative study of different samples. We chose to include compacted samples for this study because sREVs for higher porosity samples falsely convey the impression that high-resolution images of small volumes provide the best possible parameter quantification since they are segmented reliably. The greyscale method is also useful for datasets where larger scale processes are to be tracked and resolution is necessarily low, i.e. segmentation is even more difficult (Yang et al., 2017).

## 2. Materials and methods

### 2.1. Sample selection and image acquisition

Hod chalk (North Sea Basin) samples with a diameter of ~500 µm were collected from drill cuttings (Sample HC #16) and core material (Samples HC #72 and HC #70). The pore structure was mapped by X-ray holotomography, using the setup at the ID22 beamline (29.49 keV) at the European Synchrotron Research Facility (ESRF) in Grenoble, France (Cloetens et al., 1999; Vilanova et al., 2013). Samples were imaged dry and in air. The conical beam allows recording the same location in a sample at several levels of resolution, by adjusting the distance between the sample and the detector. Volume images for three samples at submicrometer resolution (100, 50 and 25 nm voxel dimension) were reconstructed from 1999 radiographs (360° rotation, 0.5 s exposure) using the holotomography reconstruction method (Cloetens et al., 1999). Some of these reconstructions were published in a previous study (Müter et al., 2014). In addition, five positions in Sample HC #70 were evaluated at 25 nm voxel resolution. This was realized by sequentially moving the sample vertically by 200 µm after each scan.

### 2.2. Image processing

All processing and analysis were performed with software custom written in Python v. 2.7 (van Rossum and Drake, 2001), using the libraries, Numpy v. 1.9, Scipy v. 0.14 (Oliphant, 2007) and Fabio v. 0.2 (Knudsen et al., 2013). Image processing was performed post reconstruction, aiming at preserving high frequency signal information. Datasets with a coherent intensity distribution were acquired by dividing the datasets into blocks of 128 slices and aligning the mode of the underlying intensity distribution. Deviations from a cylindrical sample shape resulted in reconstructions of uneven background that we compensated for, using a standard high pass filter in the Fourier domain. Ring artefacts were eliminated following the approach of Jha et al. (2014).

Signal noise was treated as Gaussian (white noise). The noise level was estimated as a lower boundary estimate from regions of low signal variation and used to restore the noise free signal with three dimensional, nonlocal means denoising (Buades et al., 2005; Coupé et al., 2008). We used only minimal patches, with a radius of one voxel, to preserve as much fine structure in the signal as possible. Images of crystalline structures are inherently piecewise constant. We used this characteristic to remove the remaining weakly correlated artefacts by updating the similarity estimate by the denoising output once for datasets with 50 nm or 100 nm voxel resolution (Fig. 1a). The increase in artefacts at higher resolution required two additional updates of the similarity estimate for datasets with 25 nm voxel resolution. A detailed explanation of the method is published elsewhere (Bruns et al., 2017).

The voxel resolution used during reconstruction was higher than the optical resolution of the imaging system. Consequently, the reconstruction provides a blurred representation of the chalk sample, requiring sharpening to avoid biasing the analysis by blurred surface voxels. Yet, greyscale analysis requires all data to be intact, prohibiting the use of image enhancement by linear filtering. We decided to treat the problem as a deconvolution problem instead. Deconvolution seeks to invert the blurring of the signal during image formation. Thus, the filter does not alter the average greyscales in the image but the frequency spectrum. To operate properly it requires a decent estimate of the point spread function. Calcite crystals in the reconstructions provide information for the undisturbed transition between foreground and background. At the edges of the calcite particles, the first image derivative characterizes the full width at half maximum (FWHM) of the point spread function (PSF), i.e. the physical image resolution. Using that information, the PSF was approximated to be constant and three-dimensional Gaussian in shape with a standard deviation ($\sigma$) of 1.7 voxels. Voxel resolution of 100, 50 and 25 nm correspond to optical resolution of 400, 200 and 100 nm, based on the FWHM of the PSF because FWHM $\approx 2.355\sigma$. Deconvolution was performed using a blockwise Python implementation of the ADM2TVL2 solver, provided with the FTVd package by Wang et al. (2008). The previous denoising step allowed minimizing regularization during deconvolution and put maximum weight on data fidelity instead (model parameter $\mu = 1000$), i.e. information on surface roughness is preserved and not lost by the total variation regularization (cf. Fig. 1a). For standard absorption tomography, reconstructed with filtered backprojection, deconvolution can be less suited than it is for holotomography reconstructions. In the latter case the PSF covers a volume of several voxels which allows for a decent image based characterization of the PSF whereas in the former case the PSF is often very narrow, i.e. spatial resolution and voxel resolution are already very similar. For analysis, the deconvolved datasets were transferred to a density based representation of the chalk sample, as discussed in the next section because all image processing steps before this step may also be considered a general part of any segmentation based analysis.

## 3. Results and discussion

### 3.1. Material density estimation

#### 3.1.1. Greyscale approaches for porosity quantification

The biological genesis of chalk results in a structure decidedly finer than can be represented on a 25 nm grid. Therefore, a high percentage of the voxels is affected by the partial volume effect, i.e. the intensity of the voxel represents a mixture of the linear attenuation coefficients for void and solid. Without the presence of significant amounts of other minerals, we expect all intermediate grey values of the voxels to be a linear combination of the attenuation of air and the calcite phase, after deconvolution, as is quite common (Jouini et al., 2014; Ketcham and Carlson; Taud et al., 2005). For this interpretation of the observed attenuation coefficients to be valid, we require either a monochromatic beam, i.e. a beam that is not subject to beam hardening, or hard X-ray radiation with energy $> 100$ keV because the linear attenuation of the material depends on its electron density as well as the effective atomic number of the observed compounds (Dyson, 1990; Teles et al., 2016). With synchrotron radiation, the former condition is fulfilled and although we do not have access to the subvoxel morphology of the material, we can at least estimate the local porosity, i.e. the porosity within a single voxel. We can expect, that incorporating this information in an analysis of petrophysical parameters reduces the error made, compared with an analysis of segmented datasets.

A well-established experimental method for porosity estimation from tomography measurements is based on the use of contrast agents and dual scans. It was developed by Withjack (1988) and has been applied to carbonate rocks until now (Teles et al., 2016; Agbougun et al., 2013; Fusi and Martinez-Martinez, 2013; Hussein et al., 2015; Mayo et al., 2015; Lin et al., 2016). In 2014, Jouini et al. (2014) performed a multiscale porosity analysis of carbonate rock without having dual scans available. They observed bimodal intensity histograms and segmented their images with a third uncertain phase that they interpolated linearly. Taud et al. (2005) presented a very promising approach for the porosity analysis of core data with poorly resolved material phases, where the intensity histogram of reconstructed grey values resulted in a unimodal distribution. They estimated porosity by identifying the CT number of the most prominent phase and interpolating to zero. This demonstrates that repeated measurements to access the den-

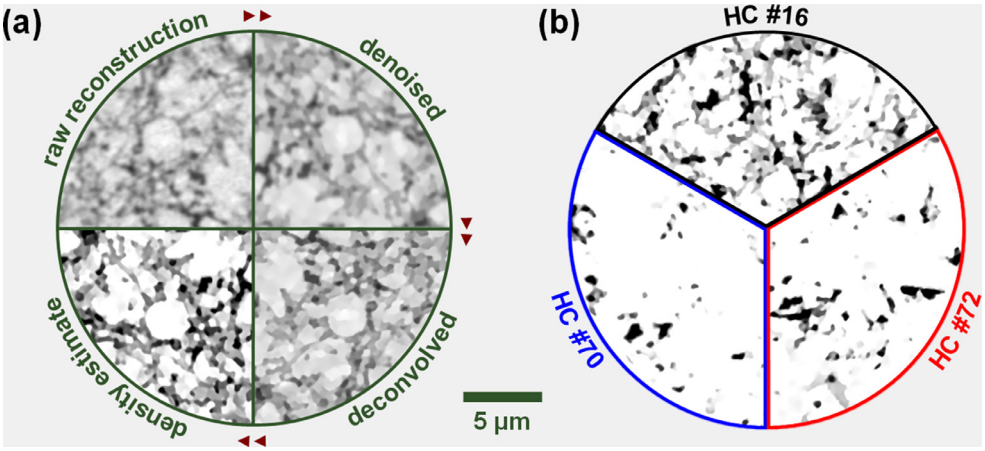


**Fig. 1.** **(a)** Stages in the image processing routine for Sample HC #16 and **(b)** close up views at 50 nm voxel resolution for the 3 samples analyzed **(b)**. Density estimates for HC #16, which is a porous chalk, and HC#70 and HC #72, which are compacted. White represents the solid phase, black, the void phase. Grey voxels are partial volume voxels containing both solid and void phase. They were assigned a porosity value by linear interpolation.

sity of a material that is basically composed of two phases are beneficial but is not necessarily essential. Yet, because only the endpoint for the density estimation is evaluated, this approach relies on having a fixed zero point and knowing the exact relationship between voxel intensity in the image and linear attenuation coefficients in the sample. When the sample extends uniformly beyond the reconstructed volume, grey values in the reconstruction are shifted by an offset and cannot be related directly to the absorption properties in the observed voxel. Often it is possible to identify regions that can be safely assigned to either void or material phase and internal calibration of average grey values can then be performed to set up interpolation points for porosity estimation or recovering the linear attenuation coefficients. However, the sheer abundance of partial volume voxels in the samples observed only provided very poor internal calibration so we had to revert to an alternative approach to extract interpolation points for the analysis.

Identifying phase ratios from reconstructed images that are severely affected by the partial volume effect is also a well-known challenge in medical magnetic resonance imaging (MRI), especially in the analysis of brain tissue (Tohka et al., 2004). Here, differentiating and quantifying grey matter, white matter and cerebrospinal fluid, with a hard segmentation approach, can yield volume errors of up to 60% (Niessen et al., 1999). The quantification problem is often addressed with a parametric statistical model that considers a Gaussian intensity model for the tissues and mixtures of tissues (Balafar, 2014; Van Leemput, 2003). Optimizing these models by expectation-maximization yields soft segmented images, a Gaussian mixture model.

#### *3.1.2. Gaussian mixture model for submicrometer resolution images of chalk*

Our approach to density quantification makes use of the statistical methods devised in medical MRI to identify the mean intensity of a solid and void phase in the chalk reconstructions (Van Leemput, 2003). Notably, denoising results for our data were good enough, that using a statistical model with additional spatial priors did not improve the model fit. We ended up identifying the void and material phase using a histogram based Gaussian mixture model with no spatial correlation. It requires the following assumptions:

i. The dominant solid phase in the mixture model is calcite.
ii. The phase of lowest X-ray attenuation is void.
iii. All intermediate grey values result from voxels that contain both calcite and void so are modelled as dependent mix phases.
iv. Any phase of higher mean intensity than the calcite phase is free and is assumed to represent accessory minerals, such as barite or pyrite (Sørensen et al., 2012).

Mixed phases can take any mixing fraction and proportion. Dependence is expressed by constraining the standard deviation of the Gaussian to be related to the standard deviation of the calcite and the void phase according to its mixing fraction. The model is initialized using k-means clustering (Lloyd, 1982) and optimized by expectation-maximization (EM) (Dempster et al., 1977). For an efficient implementation of the EM algorithm, we used histogram data that were truncated to cover 99.98% of the voxels and split into 5000 bins.

As long as the resolution of the imaging system is sufficient to fulfil the first assumption, the approach allows identification of the first moment of a void phase and a calcite phase without relying on the reconstructions having the same processing history. Assigning a porosity value to each voxel is now a simple task of linear interpolation. To maximize the comparability, we heuristically chose a model of seven Gaussian distributions because with seven Gaussian functions, the porosity estimate reaches a first plateau and all histograms are fitted with a single high intensity phase and four mixed phases, as shown in Fig. 2, for a characteristic fit.

While it is possible to extend the approach to materials that contain multiple mineral phases, this cannot be done with intensity information alone. Doing so would require incorporating spatial information in the process to identify the mineral phases that make up the mixed state of each individual voxel. This will severely increase the computational demand as well as the dimensionality of the problem and may only be worthwhile for imaging of dynamic processes for marginally resolved samples where it is not possible to perform imaging experiments at multiple energies.

### *3.2. Porosity analysis*

#### *3.2.1. Origins of variance considered*

After assigning a local porosity value to each voxel, estimating the porosity becomes straightforward. As in segmented binary datasets, porosity is provided by the expected value of a region of interest or the sample as a whole. For most practical applications of parameter prediction by X-ray imaging methods, quantification of the overall reservoir or aquifer characteristics is more useful than single characterizations of high accuracy. Evaluating the precision of our parameter estimates is therefore of prime concern. Naturally, heterogeneities on length scales of centimeters or

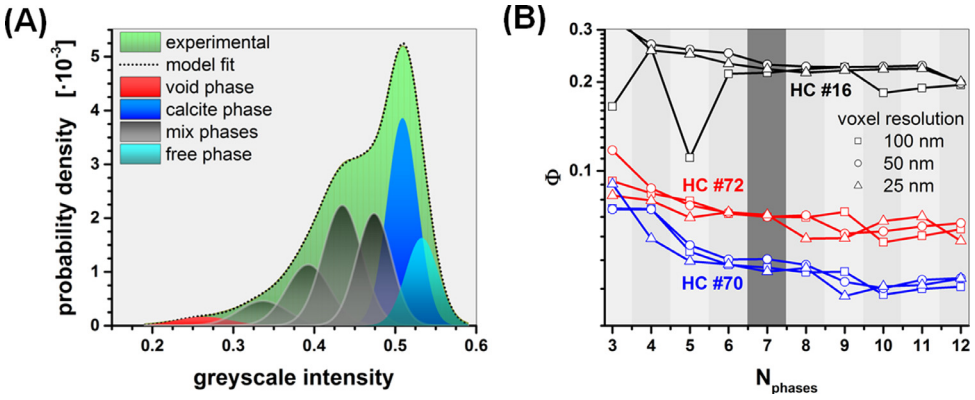


**Fig. 2.** **(a)** An example fit to a histogram of data from Sample HC #16 at 50 nm voxel resolution using a Gaussian mixture model with seven phases. The fit includes Gaussian distributions to represent the void phase (red), the calcite phase (blue), a phase called the free phase that represents high density minerals such as pyrite and barite (pale blue) and four dependent mixed phases (grey); **(b)** the dependence of the macroscopic porosity estimate on the number of peaks ($N_{phases}$) used in the Gaussian fitting. The grey bar marks the results used for this study. (For interpretation of the references to colour in this figure legend, the reader is referred to the web version of this article.)

even meters are a major limitation in digital rock physics that cannot be addressed without excessive sampling. However, statements about the bulk characteristics of the rock are definitely possible (Kynde et al., 2016) and the work of Yoon and Dewers (2013) illustrated that even with the spatial restrictions of FIB-SEM, decent precision can be expected for open pore networks. Measures that are sensitive to the shape and connectivity of the pore system require larger volumes than are typically recorded at such high resolution. Müllner et al. (2014) demonstrated this on large scale, serial block face scanning electron microscopy recordings of man-made polymer monoliths, which are presumably more homogeneous than natural porous media where the distribution of void and solid are quite random.

How representative is a micrometer length scale snapshot of a notoriously heterogeneous sample, such as chalk, and how precise can the object that is imaged be recovered given the available imaging setup? We have addressed these questions by evaluating three potential origins of variance, reported as relative standard deviation (RSD), evaluated as:

i. **Interresolution** variability: where features are insufficiently resolved at lower resolution; this parameter is expected to change dramatically when compared with higher resolution estimates.
ii. **Intersample** variability: the five locations evaluated for sample HC #72 provide us with basic insight about sampling related variability. This parameter represents heterogeneities in a single drill cutting that are one length scale higher than the imaging length scale.
iii. **Intrasample** variability: decomposing each reconstruction into sets of nonoverlapping subvolumes quantifies heterogeneities that can be captured on the imaging length scale and associated finite size effects. Care has to be taken when this parameter is used for formulating a statistically representative elementary volume. It can only be seen as a lower boundary estimate because subvolumes are still spatially correlated.

### 3.2.2. Resolution dependence

Fig. 3a presents the results of our analysis for macropore porosity (Φ). One sample (HC #16) is comparable in porosity to the Cretaceous Selma chalk examined by Yoon and Dewers (2013) whereas the other two samples (HC #72 and HC #70) are more compacted (Fig. 1b). Müter et al. previously provided a segmentation based analysis of the analysed materials (Müter et al., 2014). They observed a pronounced resolution dependence of the macropore porosity estimate reporting porosities of 0.400, 0.302 and 0.280 for Sample HC #16 at 100 nm, 50 nm and 25 nm voxel resolutions using a dual filtering approach followed by Otsu segmentation (Müter et al., 2012). The results obtained with the image processing routine used for this study are comparable. Otsu segmentation after image deconvolution suggests respective porosities of 0.340, 0.303 and 0.267 for the same material. Such pronounced segmentation errors complicate any further analysis. The error incurred by selecting a statistical model to interpolate the greyscales is smaller. With greyscale analysis we found a considerably lower porosity of 0.215, 0.229 and 0.222 for the above voxel resolutions. The porosity estimated from core log data was reported even lower with 0.142. For Sample HC #70 and HC #72 core plug experiments suggested a Φ of 0.052 and 0.071. Müter et al. reported indistinguishable values of 0.040 and 0.043 for the two samples. Greyscale analysis provided definite differences in the average porosity yielding an average Φ of 0.049 for HC #70 and 0.072 for HC #72.

In summary, the porosity estimated from the greyscale analysis does not change systematically with image resolution. The average interresolution RSD ($RSD_{res}$) is only 3%. In contrast, the intersample RSD ($RSD_{inter}$) provides an uncertainty of 11% to the estimate of porosity in Sample HC #70. This is comparable to the worst intrasample variability ($RSD_{intra}$) observed for HC #70 suggesting that the precision of a porosity estimate using submicrometer resolution volume imaging is dominated by the spatial restrictions of the imaging system and not the resolution as such.

### 3.2.3. Statistical representative elementary volume

Decomposing the sample in nonoverlapping subvolumes provides the option to deduce the intrasample variability (Fig. 3a, right panel) for predicting statistical representative elementary volumes. The uncertainty curves align well for the different voxel resolutions and span a sufficient range of volumes for reading out the sREV for the bulk matrix material directly. From a single reconstructed volume Sample HC #16 cannot be characterized at the pore scale with better precision than 3% RSD because it is limited by larger scale heterogeneities. An arbitrary but frequently used precision of 10% RSD is already reached by sampling a cubic volume of 5.5 µm edge length. For the compacted samples HC #70 and HC #72 a larger volume of at least ~15 µm edge length is required for a comparable precision. Two of the thirteen evaluations captured higher scale heterogeneities; these are Sample HC #70 at 100 nm voxel resolution which shows an increased sREV of ~70 µm edge length and Sample HC #70 at 25 nm voxel resolution in location **d** which contains an easily visible fracture (not shown).

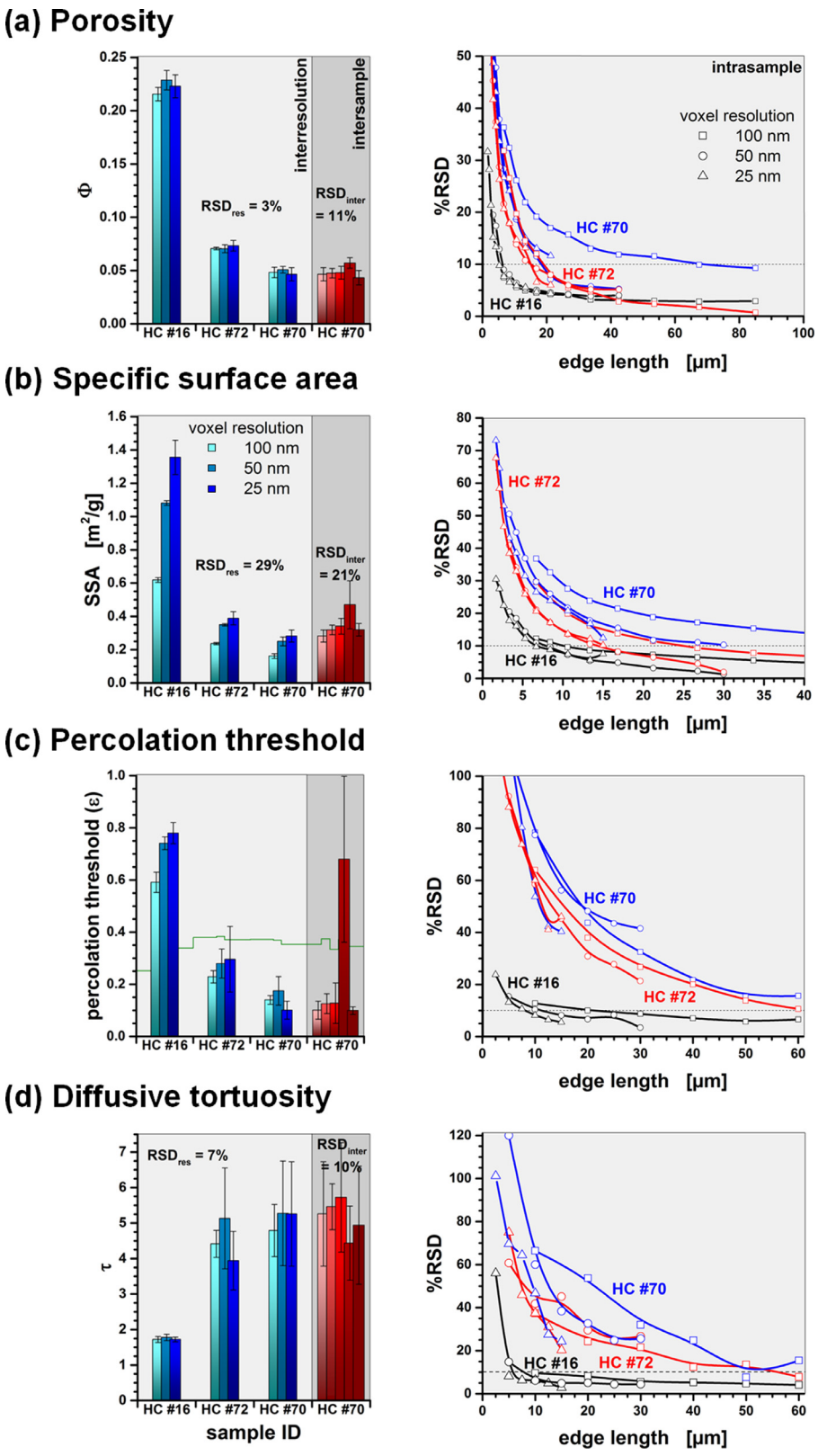


**Fig. 3.** Compilation of the greyscale measurements acquired for this study. **(a)** Statistical analyses for porosity, **(b)** specific surface area **(c)**, percolation threshold **(d)** and diffusive tortuosity were performed over a range of voxel resolutions (blue columns; pale blue, 100 nm; medium, 50 nm; dark, 25 nm) and for Sample HC #70 (red columns) at different positions within a chip of core material. Error bars in the bar chart are the standard deviation of the measurement, acquired by dividing the reconstructions into eight nonoverlapping subvolumes. Finite size effects were assessed by subdividing the reconstructions further and estimating the precision of the measurement from the relative standard deviation between these subvolumes (right plots). For diffusive tortuosity, the RSD has been adjusted for the variance between random walks by running calibration experiments with 16 repetitions for each reconstruction. The green line in **(c)** corresponds to the porosity of the Otsu threshold that would segment the volume image to a binary image. (For interpretation of the references to colour in this figure legend, the reader is referred to the web version of this article.)

### 3.3. Specific surface area

#### 3.3.1. Two point correlation function for greyscale images

A specific surface area (SSA) estimated from tomographic reconstructions is necessarily smaller than a surface area estimated by BET measurements. An image with well resolved grains may only show a small error but without molecular resolution there will always be unresolved features and defects in the structure. Small grains that contribute the most to the SSA are among the first features to be lost to the partial volume effect limiting an image analysis based SSA of chalk to comparative statements.

In a greyscale image there is no clearly defined interface between material and void phase. Thus, if we aim to relate the observation to a surface area a statistical approach is required. In a segmented dataset the two point correlation function provides one option for estimating the surface area of random porous materials (Yoon and Dewers, 2013; Berryman and Blair, 1986; Berryman and Blair, 1987; Yeong and Torquato, 1998) statistically. The function is defined as the probability of finding two points in the void phase at a given distance, $r$. As $r$ approaches zero, the slope of the correlation function provides a measure of the internal sample surface area per unit volume, $S_V$ as

$$S_V = \lim_{r\to 0} -k f'(r), \tag{1}$$

where $f'(r)$ is the first order derivative of the two point correlation function and $k$ represents a constant that is 6 in the case, where a three dimensional, discrete, cubic lattice is considered (Yeong and Torquato, 1998). A $k$ of 4 recovers the area of a continuous surface and results are in accordance with surface areas estimated by the marching cubes algorithm (Berryman and Blair, 1986; Berryman and Blair, 1987). In a binary dataset, the two point correlation function is equivalent to a linear transformation of the autocorrelation function. The idea dates back to Debye et al. (1957), who calculated specific surface areas of random porous materials from small angle X-ray scattering data. In a two phase medium, this is a binary case because fluctuations in electron density at the atomic scale are not visible at small angles.

In a greyscale image, the autocorrelation function is (usually) not an exponentially decaying function, i.e. the greyscale distribution is not entirely random and the surface area cannot be estimated with the correlation function approach of Berryman and Blair (1986, 1987). In other words, the material distribution in each partial volume voxel is not random but part of a connected open pore network. However, we do know that, when the local porosity of a voxel is between 0 and 1, surface area needs to be present. Given that we are considering an open pore network, the simplest structure that realizes a neighboring voxel of lower porosity is a tapering flow path. This is also the structure with the lowest possible surface area required to explain the observed image. If we now assume that the flow path is aligned with the connecting vector, Bayes' theorem can be applied to find the probability of finding two points located in the void phase. The result is a two point correlation function reformulated for greyscale images.

A step-by-step derivation starts with the prior probability of being at a position in the void phase $p_1$ given any voxel $a$. The single point probability of finding void phase corresponds directly to voxel level porosity. Thus:

$$p_1(a) = \varepsilon(a), \tag{2}$$

where $\varepsilon$ denotes the local porosity at voxel $a$. We assume a nearby higher density voxel $b$ to be connected to $a$ by a tapering flow path in the direction of the connecting vector with length, $r$. Given the simplified scenario of a tapering flow path, the probability of the vector also ending in the void phase is conditional on $a$:

$$\lim_{r\to 0} p_1(b|a) = \frac{p_1(a|b)\cdot\varepsilon(b)}{\varepsilon(a)} = \frac{\varepsilon(b)}{\varepsilon(a)}, \tag{3}$$

because in the tapering flow path model the conditional probability of finding a void voxel when moving from a higher density voxel to a lower density voxel, $\lim_{r\to 0} p_1(a|b)$, describes a trajectory along a widening flow path; it is obviously one. Thus, the joint probability of both voxels being in the void phase $p_{11}$ is determined by the higher density voxel, $b$:

$$\lim_{r\to 0} p_{11}(a\cap b) = p_1(b|a)\cdot p_1(a) = \varepsilon(b) \tag{4}$$

and the two point correlation function for a surface area estimate from greyscale data is consequently expressed as the expected value of the minimum function:

$$f(r) = \langle \min(\{\varepsilon(\mathrm{x}), \varepsilon(\mathrm{x}+\mathrm{r})\})\rangle. \tag{5}$$

The correlation function $f(r)$ modified for greyscale porosity values is an exponentially decaying function that is valid for small distances. Without further information about the available subvoxel surface the assumption of a tapering flow path cannot be expected to provide an accurate value for the SSA but only a value that relates to this property by providing a lower boundary estimate. This cannot prevent resolution bias of the parameter estimate but allows extracting a parameter from the greyscales that relates to the surface area. Thus, greyscale analysis may be used comparatively or in studying dynamically evolving systems (Yang et al., 2017) as long as imaging conditions are not changed.

#### 3.3.2. Resolution dependence and model study

Fig. 3b illustrates the specific surface area estimates calculated by using Eq. (5) as correlation function in Eq. (1). Values are reported for $k=6$ and by approximating the slope of the correlation function via the finite difference as $f'(r) \approx f(0)-f(1)$. Unit conversion from $m^2/m^3$ to chalk surface area per unit of mass ($m^2/g$) was performed by assuming a density of 2.71 $g/cm^3$ for calcite. It is evident that, in contrast to the porosity estimate, the accuracy of the surface area estimate depends heavily on the resolution of the imaging system – although, especially for the compacted samples, HC #70 and HC #72, with diminishing returns for doubling the spatial resolution.

Although accuracy is not our main concern, some basic insights how the presence of partial volume voxels affects different imaged based parameter estimates may be gained by performing a simple downscaling study on a model rock system. For this purpose we used a segmented volume image of Upper Maastrichtian chalk with 40.5 nm voxel resolution as a ground truth dataset because it contained plenty of well resolved calcite crystals of varying size (Fig. 4a). It is easier to study this type of chalk via segmentation than it is to study Hod chalk because grain sizes are larger. This is evident by a smaller SSA at higher porosity for the benchmark sample compared to Sample HC #16. Downsampling of the binary model was performed by volume averaging which solely simulates the partial volume effect and ignores any other image degradations. Fig. 4c illustrates how the error of the SSA estimate develops for an Otsu segmentation, a segmentation at the 50% porosity level and the greyscale approach. Herein, the latter two approaches performed similarly well (or rather poor) providing an SSA estimate of less than 10% relative error for a downsampling factor $\leq 3$ (equivalent to a voxel size of 121.5 nm). With moderate downsampling the error in the Otsu segmented dataset was dominated by the misplaced threshold resulting in an overestimated SSA for the benchmarked sample.

It is thus no surprise that SSA values for the samples scatter wildly depending on the technique used. At 25 nm voxel resolution *Müter* et al. reported an SSA of 2.1 $m^2/g$ for Sample HC #16

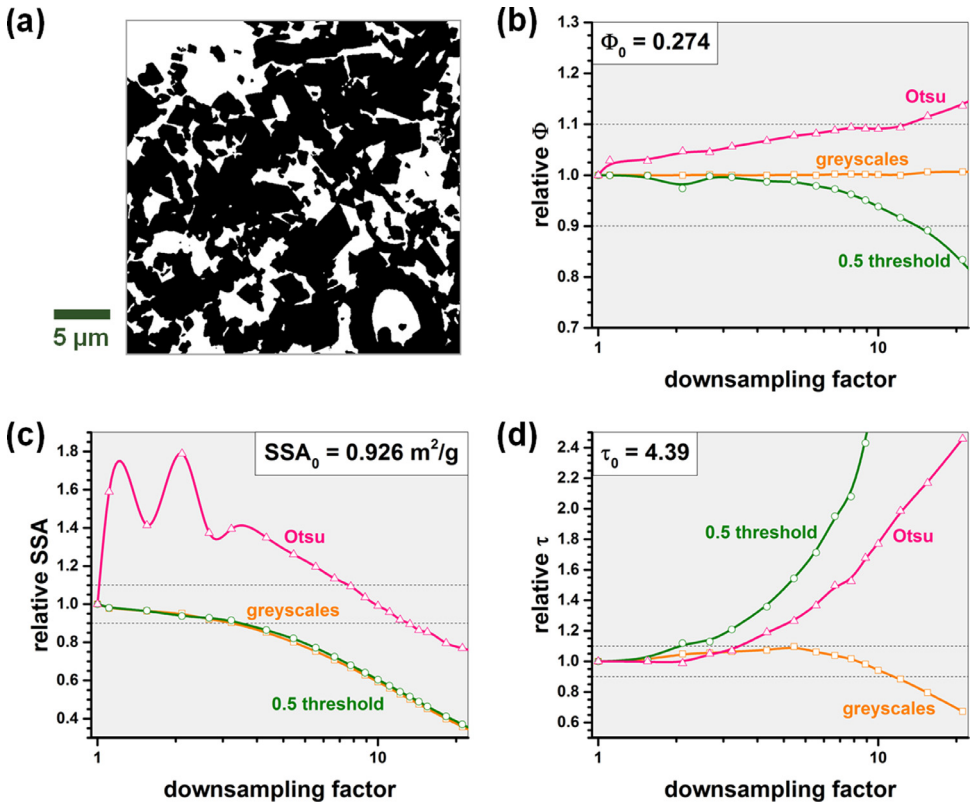


**Fig. 4.** **(a)** Slice through a binarized sample of Upper Maastrichtian Chalk used for studying the effects of downsampling via volume averaging on **(b)** porosity, **(c)** specific surface area and **(d)** tortuosity. The size of the dataset before downsampling was $732 \times 732 \times 732$ voxels at 40.5 nm voxel resolution. White denotes void space with porosity 1, black denotes material phase with porosity 0. The downsampling factor refers to multiples of the initial voxel resolution. Results for greyscale analysis (orange) segmentation via Otsu thresholding (pink) and thresholding at 0.5 porosity (olive) are shown relative to the parameter estimate provided without downsampling ($\Phi_0$, $SSA_0$, $\tau_0$). Dashed lines delineate a 10% margin of error. (For interpretation of the references to colour in this figure legend the reader is referred to the web version of this article.)

and 0.22 $m^2/g$ for sample HC #70 and HC #72 (Müter et al., 2014). From greyscale analysis we found a lower SSA of 1.4 $m^2/g$ for Sample HC #16 and a higher SSA of 0.28 $m^2/g$ for Sample HC #70 and 0.39 $m^2/g$ for Sample HC #72, whereas BET measurements suggest a SSA of 7.7 $m^2/g$ for Sample HC #16 and 0.76 $m^2/g$ for samples HC #70 and HC #72. Evidently, greyscale analysis cannot prevent resolution bias of the SSA estimate without considering a more complex system for subvoxel surface area but still enables extracting a parameter from the greyscales that relates to the surface area.

### 3.3.3. Statistical representative elementary volume

A poor accuracy does not imply poor precision or repeatability. Curves for intrasample variability at 50 nm voxel resolution provide a decent continuation of the curves resulting from the measurements at 25 nm voxel resolution (Fig. 3b, right panel). This suggests that the sREV for specific surface area increases with decreasing porosity. For Sample HC #16 the 10% RSD criterion is met for a volume with a ~7 µm edge length and at an edge length of 14.5 µm for Sample HC #72. The lowest porosity Sample HC #70 requires a sampled volume of at least 30 µm edge length, which can still be covered with a spatially limited high-resolution PXCT experiment. However, the intersample variability for Sample HC #70 volume a-e of 21% is higher than it is for porosity and intrasample curves for 100 nm voxel resolution are shifted towards higher values as well. At this resolution the edge length of the sREV for Sample HC #16 is estimated to be 10 µm and 24.5 µm for Sample HC #72. This hints that higher scale heterogeneities have a larger impact on the surface area estimate than they have on the porosity estimate but the heterogeneities of the bulk matrix material are well described with sample sizes typical for high resolution PXCT in any case ($RSD_{intra}$ ≈ 1%–10% at 30 µm sample edge length). Consequently, overall precision can only be improved by broadly spaced repetitive sampling and the imaging system with the highest available resolution remains the obvious choice for image based surface characterization.

## 3.4. Diffusive tortuosity

### 3.4.1. Limitations of hard segmentations

We initially stated that fluid flow simulations in binary representations of compacted chalk are destined to fail because tiny cracks and fractures constitute important flow paths that require high resolution to be visualized and even then, are obliterated by the segmentation process. This can be illustrated by considering a percolation threshold for the analyzed greyscale images as a test for connectedness. We define this percolation threshold by the lowest value of local voxel level porosity that has to be traversed to connect two opposing faces of the reconstruction. The higher the value, the better resolved are the major flow paths in the microstructure. The measurement is not a material property but characteristic for each reconstruction. It can be expected to increase with resolution. If it is lower than the Otsu threshold that segments the volume image, a binary rock model acquired with that method would appear impermeable. The plot in Fig. 3c immediately reveals that this is the case for Sample HC #72 and HC #70. Notably, the percolation threshold does not increase but rather drops for Sample HC #70 when the voxel resolution increases from 50 nm to 25 nm. This indicates that the sampled volume is insufficient to characterize the microstructure of that material. In addition, the percolation threshold is quite volatile. For Sample HC #16, a cubic volume with an edge length of 10 µm is enough to characterize it with about 10% RSD but Sample HC #72 and HC #70 require a cubic volume of more than 50 µm edge length for a mea-

surement of comparable precision. This uncertainty carries over to the derivation of any parameter that depends on flow paths, whether it is based on binary data or greyscale data.

*3.4.2. Diffusive tortuosity simulation for greyscale images*

Diffusive tortuosity lends itself to a characterization by greyscale analysis because it can be modelled by a statistical process. It is a parameter that is sensitive to pore shape and connectivity, i.e. that we expect the sREV for diffusive tortuosity to be on a similar scale as the sREV for single phase liquid permeability and/or formation resistivity factor. Thus, we chose to characterize the diffusive tortuosity of our samples by modelling molecular diffusion with a discrete lattice random walk ($1{\cdot}10^4$ walkers, $1{\cdot}10^6$ time steps, reflective boundary conditions) in a simple cubic lattice (Nakashima et al., 2004; Nakashima and Kamiya, 2007). The tortuosity was calculated as the inverse of the slope of the mean square displacement in the final $2{\cdot}10^5$ time steps. This can only provide reasonable results when the structure is permeable, i.e. use of greyscale information is mandatory for the compacted samples. Without a clearly defined material-void interface, the reflection of a walker is a probability. Within the model assumption of a tapering flow path that was used to relate the greyscales to surface area in Section 3.3 reflections may only occur when a walker moves to a higher density voxel. We consider the displacement at each time step to be sufficiently small to apply the assumptions made for the surface area estimate to this problem as well. A walker encountered at any timestep and position needs to be in the void space with probability 1. This means that a successful walking step depends on finding another void location in location $b$ which is the conditional probability provided with Eq. (3). The probability for encountering an interface reflection $p_{\text{reflect}}$ is therefore given by:

$$p_{\text{reflect}} = \lim_{r\to 0} 1 - p_1(b|a) = 1 - \frac{\varepsilon(b)}{\varepsilon(a)}. \tag{6}$$

*3.4.3. Resolution dependence*

Fig. 4d illustrates how accurate diffusive tortuosity is recovered in the presence of partial volume voxels given the benchmark dataset considered. While segmenting the dataset at 50% porosity served reasonably well for porosity (Fig. 4b) and identical to the greyscale approach for specific surface area (Fig. 4c) it is the worst performing approach for diffusive tortuosity. The tendency to underestimate porosity results in rapid disconnection of important flow paths and the 10% error mark is already exceeded when the test volume image is downsampled by a factor of two. Otsu thresholding performs better in this specific case because for the benchmark sample this segmentation technique overestimates porosity and pores are disconnected at a later downsampling stage. Thus the error is smaller than 10% with downsampling factors $\leq 3$. With the greyscale approach pores can never be disconnected (within the benchmark experiment) but tortuosity may be underestimated once the voxels are large enough that pores start to get merged. This was first observed for a downsampling factor of 6 and an error of less than 10% was maintained up to a downsampling factor of 10.

The application to the chalk samples studied was similar promising as it did not result in an identifiable resolution dependency of the diffusive tortuosity (Fig. 3d). All values for 100 nm, 50 nm and 25 nm voxel resolution were within the expected margin of error that would result from finite size effects, i.e. greyscale information on fractures resolved at 25 nm voxel resolution is also contained in the images recorded at 100 nm resolution.

*3.4.4. Statistical representative elementary volume*

Upon inspection of the intrasample variance we see that Sample HC #16 is precisely characterized without major precision loss because of finite size effects with $\tau = 1.7$ for sample sizes $\geq 10\,\mu m$ edge length which agrees well with the sREV suggest by Yoon and Dewers (2013). Increasing the sample size further does not improve precision below 4% RSD indicating the presence of larger scale heterogeneities. Results on the compacted samples, HC #72 and HC #70, are not as clear. The intrasample variability compares well to the variability observed for the percolation threshold. At 25 nm and 50 nm voxel resolution, we cannot expect a precision considerably higher than ~25% RSD, whereas the uncertainty drops to the scale of intersample variability (~10% RSD) at 100 nm voxel resolution (Fig. 3d, right panel) for an edge length ~50 µm. This has two fundamental implications for the future analysis of permeability and further flow related parameters in compacted chalk samples. The network of flow paths is only captured representatively with sample volumes of 50 µm diameter or larger. At present this can only be accomplished (in a reasonable timeframe without making mosaics) by relaxing the resolution requirements in the data acquisition step to the point where fractures are marginally resolved. As a result, quantitative greyscale analysis cannot be avoided for deriving the petrophysical parameters of such samples. This requires further development because segmentation based characterization methods give away too much signal information.

## 3. Summary and conclusions

Characterizing the petrophysical parameters of compacted chalk samples poses a challenge to digital rock physics because of their narrow pore network. The heterogeneity of the rock requires comparably large volumes, to produce data that are representative for the structure. Given a target RSD of 10%, porosity and specific surface area of the compacted samples were not necessarily accurately but precisely characterized with a cubic region of ~20 µm and ~30 µm edge length. For diffusive tortuosity, the same criterion is only met for an edge length of ~50 µm or more. Acquiring volumes of that size at a physical resolution below 100 nm is usually not a default option in high resolution imaging methods, such as PXCT or FIB-SEM. Still, our analysis shows that the resolution power of these methods is required, to resolve the surface of the pore interface and all fractures and thin pore throats that are necessary for modelling fluid flow and material transport in pore systems, with a binary representation of the porous medium.

We demonstrated that quantitative greyscale analysis provides a viable workaround out of the dilemma of requiring both large volumes (or at least a large number of samples) and maximum resolution power whenever finite size effects outweigh potential gains in precision by higher resolution imaging. Greyscale analysis relaxes requirements in image resolution (Müter et al., 2014) for pore network related parameters and porosity analysis. This is because greyscale images maintain more of the signal information that is available in the recorded images than a segmentation based characterization. Basis for the presented quantitative analysis was a transformation to voxel level porosity that we performed by identifying the greyscale levels for calcite and void pore space with a Gaussian mixture model optimized with expectation maximization. Estimating the material density by identifying two phases allows comparing image data of differing origin. The transformed data were analyzed in terms of porosity, specific surface area and diffusive tortuosity revealing the predominant sources of variance in the image based analysis of these parameters. The precision of porosity estimates was limited by the presence or absence of higher scale heterogeneities and requires extensive sampling to be improved. As expected, the determined specific surface area largely depends on image resolution and will always be smaller than a BET surface. The precision of image based estimates for the diffusive tortuosity was found to be limited primarily by the size of

the reconstructed sample volume. This is especially problematic for heterogeneous compacted samples because without image mosaicking, the material cannot be imaged on a scale and resolution that allows quantification by segmentation. Relating the specific surface area and diffusive tortuosity to greyscale images was made possible by making a model assumption about the geometry of the unresolved open pore network, i.e. the voxels that were affected by the partial volume effect. This illustrates how typical tools for quantitative image analysis can be reformulated for material density based greyscale data with this assumption, using straightforward Bayesian theory.

Our method provides a sound approach for characterizing samples where data are at the limits of resolution so diffusive tortuosity can be derived for samples that could not otherwise be evaluated. Yet, the canny reader will have noticed that we do not discuss permeability, which is one of the key petrophysical parameters. Deriving permeability from greyscale image information is a task that is beyond the scope of this study but it is an ongoing project in our group. This paper provides the basis for that work and underlines the importance of developing greyscale measures for more complex flow path related parameters with better accuracy than our simple approach can deliver. Yet, definite conclusions can be drawn on the expected precision of a 3D imaging experiment and knowing beforehand, the expected precision of measurements in compacted samples, as a worst case scenario, provides us and other researchers with a framework for more effective planning of such experiments.

## Acknowledgements

Funding for this project was provided by the Innovation Fund Denmark and Maersk Oil and Gas A/S through the $P^3$ Project and Innovation Fund Denmark through the CINEMA Project. DANSCATT, funded by the Danish Agency for Science, Technology and Innovation, covered costs for travelling and accommodation for synchrotron beamtime. We thank S. Pedersen, D. Müter, K. N. Dalby for their help and Heikki Suhonen at the ID22 beamline at ESRF (The European Synchrotron) for technical support.

## References

Agbougun, H.M.D., Al, T.A., Hussein, E.M.A., 2013. Three dimensional imaging of porosity and tracer concentration distributions in a dolostone sample during diffusion experiments using X-ray micro-CT. J. Contam. Hydrol. 145, 44–53. http://dx.doi.org/10.1016/j.jconhyd.2012.11.008.

Andrä, H., Combaret, N., Dvorkin, J., Glatt, E., Han, J., Kabel, M., Keehm, Y., Krzikalla, F., Lee, M., Madonna, C., Marsh, M., Mukerji, T., Saenger, E.H., Sain, R., Saxena, N., Ricker, S., Wiegmann, A., Zhan, X., 2013. Digital rock physics benchmarks—part II: Computing effective properties. Comput. Geosci. 50, 33–43. http://dx.doi.org/10.1016/j.cageo.2012.09.008.

Arns, C.H., Knackstedt, M.A., Pinczewski, W.V., Lindquist, W.B., 2001. Accurate estimation of transport properties from microtomographic images. Geophys. Res. Lett. 28 (17), 3361–3364. http://dx.doi.org/10.1029/2001GL012987.

Balafar, M.A., 2014. Gaussian mixture model based segmentation methods for brain MRI images. Artif. Intell. Rev. 41 (3), 429–439. http://dx.doi.org/10.1007/s10462-012-9317-3.

Balogh, Z., Pedersen, C.S., Skovbjerg, L.L., Hassenkam, T., Johnson, E., Bechgaard, K., Benning, L.G., Stipp, S.L.S., 2009. Surface composition of fossil coccoliths from chalk. Geochim. Cosmochim. Ac. 73 (13), A82. http://dx.doi.org/10.1016/j.gca.2009.05.002.

Berryman, J.G., Blair, S.C., 1986. Use of image analysis to estimate fluid permeability of porous materials: application of two-point correlation functions. J. Appl. Phys. 60, 1930–1938. http://dx.doi.org/10.1063/1.337245.

Berryman, J.G., Blair, S.C., 1987. Kozeny-Carman relations and image processing methods for estimating darcy's constant. J. Appl. Phys. 62, 2221–2228. http://dx.doi.org/10.1063/1.339497.

Bijeljic, B., Mostaghimi, P., Blunt, M.J., 2013. Insights into non- Fickian solute transport in carbonates. Water Resour. Res. 49 (5), 2714–2728. http://dx.doi.org/10.1002/wrcr.20238.

Bruns, S., Stipp, S.L.S., Sørensen, H.O., 2017. Looking for the signal: a guide to noise and artefact removal in X-ray tomography reconstructions of Porous Geomaterials. Adv. Water Resour. 105, 96–107. http://dx.doi.org/10.1016/j.advwatres.2017.04.020.

Buades, A., Coll, B., Morel, J.M., 2005. A review of image denoising algorithms, with a new one. Multiscale Model. Simul. 4 (2), 490–530. http://dx.doi.org/10.1137/040616024.

Bultreys, T., Van Hoorebeke, Cnudde, V., 2015. Multi-scale, micro-computed tomography-based pore network models to simulate drainage in heterogeneous rocks. Adv. Water Resour. 78, 36–49. http://dx.doi.org/10.1016/j.advwatres.2015.02.003.

Cloetens, P., Ludwig, W., Baruchel, J., van Dyck, D., van Landuyt, J., Guigay, J.P., Schlencker, M., 1999. Holotomography: quantitative phase tomography with micrometer resolution using hard synchrotron radiation x rays. Appl. Phys Lett. 75, 2912–2914. http://dx.doi.org/10.1063/1.125225.

Coupé, P., Yger, P., Prima, S., Hellier, P., Kervrann, C., Barillot, C., 2008. An optimized blockwise nonlocal means denoising filter for 3-D magnetic resonance images. IEEE T. Med. Imaging 27 (4), 425–441. http://dx.doi.org/10.1109/TMI.2007.906087.

Dalby, K.N., Sørensen, H.O., Müter, D., Jha, D., da Silva, J.C., Stipp, S.L.S., 2014. From oil field to ptychography: applications of FIB-SEM in NanoGeoScience. Microsc. Microanal. 20 (S3), 316–317. http://dx.doi.org/10.1017/S1431927614003304.

Debye, P., Anderson Jr., H.R., Brumberger, H., 1957. Scattering by an inhomogeneous solid. II. The correlation function and its application. J. Appl. Phys. 28, 679–683. http://dx.doi.org/10.1063/1.1722830.

Dempster, A.P., Laird, N.M., Rubin, D.B., 1977. Maximum likelihood from incomplete data via the EM algorithm. J. R. Stat. Soc., Series B 39, 1–38.

Denk, W., Horstmann, H., 2004. Serial block-face scanning electron microscopy to reconstruct three-dimensional tissue nanostructure. PLoS Biol. 2 (11), e329. http://dx.doi.org/10.1371/journal.pbio.0020329.

Dyson, N.A., 1990. X-rays in Atomic and Nuclear Physics, second ed. Longmann, London.

Fredrich, J.T., DiGiovanni, A.A., Noble, D.R., 2006. Predicting macroscopic transport properties using microscopic image data. J. Geophys. Res. 111 (B3), B03201. http://dx.doi.org/10.1029/2005JB003774.

Fusi, N., Martinez-Martinez, J., 2013. Mercury porosimetry as a tool for improving quality of micro-CT images in low porosity carbonate rocks. Eng. Geol. 166, 272–282. http://dx.doi.org/10.1016/j.enggeo.2013.10.002.

Fusseis, F., Xiao, X., Schrank, C., De Carlo, F., 2014. A brief guide to synchrotron radiation-based microtomography in (structural) geology and rock mechanics. J. Struct. Geol. 65, 1–16. http://dx.doi.org/10.1016/j.jsg.2014.02.005.

Golab, A., Romeyn, R., Averdunk, H., Knackstedt, M., Senden, T.J., 2013. 3D characterisation of potential $CO_2$ reservoir and seal rocks. Aust. J. Earth. Sci. 60 (1), 111–123. http://dx.doi.org/10.1080/08120099.2012.675889.

Hu, Q., Ewing, R.P., Dultz, S., 2012. Low pore connectivity in natural rock. J. Contam. Hydrol. 133, 76–83. http://dx.doi.org/10.1016/j.jconhyd.2012.03.006.

Hussein, E.M.A., Agbogun, H.M.D., Al, T.A., 2015. Calibration-free quantification of interior properties of porous media with X-ray computed tomography. Appl. Radiat. Isotopes 97, 130–139. http://dx.doi.org/10.1016/j.apradiso.2014.12.016.

Iassonov, P., Gebrenegus, T., Tuller, M., 2009. Segmentation of X-ray computed tomography images of porous materials: A crucial step for characterization and quantitative analysis of pore structures. Water Resour. Res. 45 (9), W09415. http://dx.doi.org/10.1029/2009WR008087.

Jha, D., Sørensen, H.O., Dobberschütz, S., Feidenhans'l, R., Stipp, S.L.S., 2014. Adaptive center determination for effective suppression of ring artifacts in tomography images. Appl. Phys. Lett. 105, 143107. http://dx.doi.org/10.1063/1.4897441.

Jouini, M.S., Vega, S., Al-Ratrout, A., 2014. Numerical estimation of carbonate rock properties using multiscale images. Geophys. Prospect. 63 (2), 405–421. http://dx.doi.org/10.1111/1365-2478.12156.

Keller, L.M., Holzer, L., Schuetz, P., Gasser, P., 2013. Pore space relevant for gas permeability in Opalinus clay: Statistical analysis of homogeneity, percolation, and representative volume element. J. Geophys. Res. Sol. Ea. 118 (6), 1–14. http://dx.doi.org/10.1002/jgrb.50228.

Kelly, S., El Sobky, H., Torres-Verdín, Balhoff, M.T., 2016. Assessing the utility of FIB-SEM images for shale digital rock physics. Adv. Water Resour. 95, 302–316. http://dx.doi.org/10.1016/j.advwatres.2015.06.010.

Ketcham, R.A., and Carlson, W.D., Available from: http://www.ctlab.geo.utexas.edu/about-ct/artifacts-and-partial-volume-effects/ (Accessed August 2016).

Knackstedt, M.A., Latham, S., Madadi, M., Sheppard, A., Varslot, T, Arns, C., 2009. Digital rock physics: 3D imaging of core material and correlations to acoustic and flow properties. Lead. Edge 28 (1), 28–33. http://dx.doi.org/10.1190/1.3064143.

Knudsen, E.B., Sørensen, H.O., Wright, J.P., Goret, G., Kieffer, J., 2013. FabIO: easy access to 2D X-ray detector images in Python. J. Appl. Cryst. 46, 537–539. http://dx.doi.org/10.1107/S0021889813000150.

Kynde, S.A.R., Engstrøm, F., Feidenhans'l, R.K., Stipp, S.L.S., 2016. Using X-ray microtomography to obtain a 3D representation of the pore space in North Sea chalk. Energ. Fuels To *be submitted, available on request*.

Lee, J.A., 2010. Segmentation of positron emission tomography images: some recommendations for target delineation in radiation oncology. Radiother. Oncol. 96 (3), 302–307. http://dx.doi.org/10.1016/j.radonc.2010.07.003.

Lin, Q., Al-Khulaifi, Blunt, M.J., Bijeljic, B., 2016. Quantification of sub-resolution porosity in carbonate rocks by applying high-salinity contrast brine using X-ray microtomography differential imaging. Adv. Water Resour. 96, 306–322. http://dx.doi.org/10.1016/j.advwatres.2016.08.002.

Liu, J., Pereira, G.G., Regenauer-Lieb, K., 2014. From characterisation of pore-structure to simulations of pore-scale fluid flow and the upscaling of permeability using microtomography: a case study of heterogeneous carbonates. J. Geochem. Explor. 144 (A), 84–96. http://dx.doi.org/10.1016/j.gexplo.2014.01.021.

Lloyd, S.P., 1982. Least squares quantization in PCM. IEEE Trans. Inform. Theory 28 (2), 129–137. http://dx.doi.org/10.1109/TIT.1982.1056489.

Müllner, T., Zankel, A., Svec, F., Tallarek, U., 2014. Finite-size effects in the 3D reconstruction and morphological analysis of porous polymers. Mater. Today 17 (8), 404–411. http://dx.doi.org/10.1016/j.mattod.2014.07.003.

Müter, D., Pedersen, S., Sørensen, H.O., Feidenhans'l, R., Stipp, S.L.S., 2012. Improved segmentation of X-ray tomography data from porous rocks using a dual filtering approach. Comput. Geosci. 49, 131–139. http://dx.doi.org/10.1016/j.cageo.2012.06.024.

Müter, D., Sørensen, H.O., Jha, D., Harti, R., Dalby, K.N., Suhonen, H., Feidenhans'l, Engstrøm, F., Stipp, S.L.S., 2014. Resolution dependence of petrophysical parameters derived from X-ray tomography of chalk. Appl. Phys. Lett. 105, 043108. http://dx.doi.org/10.1063/1.4891965.

Mayo, S., Josh, M., Nesterets, Y., Esteban, L., Pervukhina, M., Clennell, M.B., Maksimenko, A., Hall, C., 2015. Quantitative micro-porosity characterization using synchrotron micro-CT and xenon K-edge subtraction in sandstones, carbonates, shales and coal. Fuel 154, 167–173. http://dx.doi.org/10.1016/j.fuel.2015.03.046.

Mostaghimi, P., Blunt, M.J., Bijeljic, B., 2013. Computations of absolute permeability on micro-CT images. Math. Geosci. 45 (1), 103–125. http://dx.doi.org/10.1007/s11004-012-9431-4.

Mostaghimi, P., Liu, M., Arns, C.H., 2016. Numerical simulation of reactive transport on micro-CT images. Math. Geosci. 48 (8), 963–983. http://dx.doi.org/10.1007/s11004-016-9640-3.

Nakashima, Y., Kamiya, S., 2007. Mathematica programs for the analysis of three-dimensional pore connectivity and anisotropic tortuosity of porous rocks using X-ray computed tomography image data. J. Nucl. Sci. Technol. 44 (9), 1233–1247. http://dx.doi.org/10.1080/18811248.2007.9711367.

Nakashima, Y., Nakano, T., Nakamura, K., Uesugi, K., Tsuchiyama, A., Ikeda, S., 2004. Three-dimensional diffusion of non-sorbing species in porous sandstone: computer simulation based on X-ray microtomography using synchrotron radiation. J. Contam. Hydrol. 74 (1–4), 253–264. http://dx.doi.org/10.1016/j.jconhyd.2004.03.002.

Niessen, W.J., Vincken, K.L., Weickert, J., Ter Haar Romeny, B.M., Viergever, M.A., 1999. Multiscale segmentation of three-dimensional MR brain images. Int. J. Comput. Vis. 31 (2), 185–202. http://dx.doi.org/10.1023/A:1008070000018.

Oliphant, T.E., 2007. Python for scientific computing. Comput. Sci. Eng. 9, 10–20. http://dx.doi.org/10.1109/MCSE.2007.58.

Raeini, A.Q., Bijeljic, B., Blunt, M.J., 2015. Modelling capillary trapping using finite-volume simulation of two-phase flow directly on micro-CT images. Adv. Water Resour. 83, 102–110. http://dx.doi.org/10.1016/j.advwatres.2015.05.008.

Sørensen, H.O., Hakim, S., Pedersen, S., Christiansen, B.C., Balogh, Z.I., Hem, C.P., Pasarin, I.S., Schmidt, S., Olsen, U.L., Oddershede, J., Frandsen, C., Feidenhans'l, R., Stipp, S.L.S., 2012. Non-destructive identification of micrometer-scale minerals and their position within a bulk sample. Can. Miner. 50 (2), 501–509. http://dx.doi.org/10.3749/canmin.50.2.501.

Saraji, S., Piri, M., 2015. The representative sample size in shale oil rocks and nano-scale characterization of transport properties. Int. J. Coal Geol. 146, 42–54. http://dx.doi.org/10.1016/j.coal.2015.04.005.

Shah, S.M., Gray, F., Crawshaw, J.P., Boek, E.S., 2016. Micro-computed tomography pore-scale study of flow in porous media: effect of voxel resolution. Adv. Water Resour. 95, 276–287. http://dx.doi.org/10.1016/j.advwatres.2015.07.012.

Siddiqui, S., Sarker, M.R.H., 2010. Trends in CT-scanning of reservoir rocks. Adv. Comput. Tomogr. Geomater. 189–196. http://dx.doi.org/10.1002/9781118557723.ch23.

Smith, M.M., Hao, Y., Carroll, S.A., 2017. Development and calibration of a reactive transport model for carbonate reservoir porosity and permeability changes based on CO2 core-flood experiments. Int. J. Greenh. Gas Control 57, 73–88. http://dx.doi.org/10.1016/j.ijggc.2016.12.004.

Taud, H., Martinez-Angeles, R., Parrot, J.F., Hernandez-Escobedo, L., 2005. Porosity estimation method by X-ray computed tomography. J. Petrol. Sci. Eng. 47 (3–4), 209–217. http://dx.doi.org/10.1016/j.petrol.2005.03.009.

Teles, A.P., Lima, I., Lopes, R.T., 2016. Rock porosity quantification by dual energy X-ray computed microtomography. Micron 83, 72–78. http://dx.doi.org/10.1016/j.micron.2016.02.004.

Tohka, J., Zijdenbos, A., Evans, A., 2004. Fast and robust parameter estimation for statistical partial volume models in brain MRI. NeuroImage 23 (1), 84–97. http://dx.doi.org/10.1016/j.neuroimage.2004.05.007.

Van Leemput, K., 2003. A unifying framework for partial volume segmentation of brain MR images. IEEE T. Med. Imaging 22 (1), 105–119. http://dx.doi.org/10.1109/TMI.2002.806587.

van Rossum, G., Drake, F.L., 2001. Python Reference Manual. PythonLabs, VA, USA http://www.python.org.

Vilanova, J., Laurencin, J., Cloetens, P., Bleuet, P., Delette, G., Suhonen, H., Usseglio-Viretta, F., 2013. J. Power Sources. 243, 841–849. http://dx.doi.org/10.1016/j.jpowsour.2013.06.069.

Wang, Y., Yang, J., Yin, W., Zhang, Y., 2008. A new alternating minimization algorithm for total variation image reconstruction. SIAM J. Imaging Sci. 1 (3), 248–272. http://dx.doi.org/10.1137/080724265.

Warren, J., 2000. Dolomite: occurrence, evolution and economically important associations. Earth Sci. Rev. 52 (1–3), 1–81. http://dx.doi.org/10.1016/S0012-8252(00)00022-2.

Wildenschild, D., Sheppard, A.P., 2013. X-ray imaging and analysis techniques for quantifying pore-scale structure and processes in subsurface porous medium systems. Adv. Water Resour. 51, 217–246. http://dx.doi.org/10.1016/j.advwatres.2012.07.018.

Withjack, E.M., 1988. Computed tomography for rock-property determination and fluid-flow visualization. SPE Formation Eval. 3 (4), 696–704. http://dx.doi.org/10.2118/16951-PA.

Yang, Y., Hakim, S., S., Bruns, S., Uesugi, K., Dalby, K.N., Stipp, S.L.S., Stipp, Sørensen, H.O., 2017. Wormholes grow along paths with minimal cumulative surface. Sci. Adv. *Submitted,* https://arxiv.org/ftp/arxiv/papers/1704/1704.01062.pdf.

Yeong, C.L.Y, Torquato, S., 1998. Reconstructing random porous media. Phys. Rev. E. 57, 495–506. http://dx.doi.org/10.1103/PhysRevE.57.495.

Yoon, H., Dewers, T.A., 2013. Nanopore structures, statistically representative elementary volumes, and transport properties of chalk. Geophys. Res. Lett. 40 (16), 4294–4298. http://dx.doi.org/10.1002/grl.50803.

Zakirov, T.R., Galeev, A.A., Korolev, E.A., Statsenko, E.O., 2016. Flow properties of sandstone and carbonate rocks by X-ray computed tomography. Curr. Sci. 110 (11), 2142–2148.

Zhang, D., Zhang, R., Chen, S., Soll, W.E., 2000. Pore scale study of flow in porous media: Scale dependency, REV, and statistical REV, Geophys. Res. Lett. 27 (8), 1195–1198. http://dx.doi.org/10.1029/1999GL011101.

Zhu, W.C., Liu, J., Elsworth, D., Polak, A., Grader, A., Sheng, J.C., Liu, J.X., 2007. Tracer transport in a fractured chalk: X-ray CT characterization and digital-image-based (DIB) simulation. Transp. Porous Med. 70 (1), 25–42. http://dx.doi.org/10.1007/s11242-006-9080-5.